Salvador, FJ.; Carreres, M.; Garcia Tiscar, J.; Belmar-Gil, M. (2021). Modal decomposition of the unsteady non-reactive flow field in a swirl-stabilized combustor operated by a Lean Premixed injection system. Aerospace Science and Technology. 112:1-13. https://doi.org/10.1016/j.ast.2021.106622

# Modal Decomposition of the unsteady non-reactive flow field in a swirl-stabilized combustor operated by a Lean Premixed injection system

**Salvador, F.J., Carreres, M. (*), García Tiscar, J., Belmar-Gil, M.**

CMT-Motores Térmicos, Universitat Politècnica de València

Camino de Vera s/n, E-46022 Spain

(*) Corresponding author:

Dr. Marcos Carreres, marcarta@mot.upv.es

CMT-Motores Térmicos, Universitat Politècnica de València

Camino de Vera s/n, E-46022 Spain

Telephone: +34 963 876 555

## ABSTRACT

This work is focused on the numerical study of low-order coherent structures of a high-swirled laboratory-scaled combustor operated by a Lean Premixed (LP) injection system in non-reacting conditions through different flow modal decomposition techniques. This will provide valuable insight into the time-spatial modal structure detecting coherent spatial patterns. Experiments suggest the appearance of a self-excited hydrodynamic instability characterized by a single dominant frequency. On the one hand, the dominant pulsating energy components associated with the Precessing Vortex Core (PVC) are identified through the application of a Proper Orthogonal Decomposition (POD) to the instantaneous velocity field. On the other hand, Dynamic Mode Decomposition (DMD) is proven to effectively highlight the relation between the frequency of the most dominant unsteady vortex structures and their spatial distribution within the combustor. Since DMD analysis generates a global frequency spectrum in which each mode corresponds to a specific discrete frequency, its application has been demonstrated to be more efficient than POD when dealing with temporally coherent problems. In this way, the DMD technique has proved to be a robust and systematic method that can give accurate and consistent interpretations of the periodic physics underlying hydrodynamic instabilities in the combustor studied in the present investigation.

Salvador, F.J., Carreres, M., García-Tíscar, J., Belmar-Gil, M., "Modal decomposition of the unsteady non-reactive flow field in a swirl-stabilized combustor operated by a Lean Premixed injection system", Aerospace Science and Technology 112:106622 (author version).

doi: 10.1016/j.ast.2021.106622

**KEYWORDS**

Swirling flow, LES, PVC, POD, DMD

**LIST OF NOTATION**

$D_{ext}$ external diameter of the swirler exit

$f$ frequency of a given structure

$M$ number of scalar flow magnitudes used in POD

$N$ number of temporal snapshots

$R_{ext}$ outer radius of injection

$r$ grid-scale factor

$St$ Strouhal number

$S_W$ swirl number

$\boldsymbol{U}$ POD left-singular vectors

$U_{Swirler}$ bulk velocity from the swirler

$\boldsymbol{V_1}$ flow field POD matrix

$\boldsymbol{V_2}$ flow field DMD matrix

$\boldsymbol{W}$ POD right-singular vectors

$y^+$ non-dimensional boundary layer distance

*GREEK SYMBOLS*

$\lambda$ DMD modal eigenvalue

$\boldsymbol{\Phi}$ DMD modal shape

$\phi$ swirl vane angle

$\Sigma$ POD diagonal matrix

$\boldsymbol{\psi_i}$ POD spatial modes

$\Delta t$ time step

$\tau$ reference timescale

$\tau_{PVC}$ precession period of the central vortex

$\tau_{rot}$ rotation time scale associated with the Vortex Breakdown Bubble

*ABBREVIATIONS*

Salvador, F.J., Carreres, M., García-Tíscar, J., Belmar-Gil, M., "Modal decomposition of the unsteady non-reactive flow field in a swirl-stabilized combustor operated by a Lean Premixed injection system", Aerospace Science and Technology 112:106622 (author version).

doi: 10.1016/j.ast.2021.106622

| | |
|---|---|
| AMR | Adaptive Mesh Refinement |
| CFD | Computational Fluid Dynamics |
| CRZ | Central Recirculation Zone |
| DMD | Dynamic Mode Decomposition |
| ICE | Internal Combustion Engine |
| LDI | Lean Direct Injection |
| LES | Large Eddy Simulation |
| LP | Lean Premixed |
| PIV | Particle Image Velocimetry |
| POD | Proper Orthogonal Decomposition |
| PSD | Power Spectral Density |
| PVC | Precessing Vortex Core |
| SVD | Singular Value Decomposition |
| RMS | Root Mean Square |
| VBB | Vortex Breakdown Bubble |

## 1. INTRODUCTION

Aeronautical gas turbine engines present the main challenge of increasing the efficiency of the cycle while keeping the pollutant emissions below stringent restrictions [1]. This has led to the design of new injection-combustion strategies working on relatively problematic operating points such as those close to the lean extinction limit. In this context, the Lean Direct Injection (LDI) concept has emerged as a promising technology to reduce oxides of nitrogen ($NO_x$) for next-generation aircraft gas turbine engines [2].

Swirling flows are commonly found in most practical applications such as gas turbine combustors, swirl burners, furnaces, spraying machines, whirlpools, cyclone separators and vortex shedding from aircraft wings [3]. The effect of the swirl intensity in swirling jets is well defined in the literature [3-5]. The swirl number ($S$), defined as the ratio of the axial flux of angular momentum to the product of the axial momentum flux and a characteristic radius [6], is usually employed to quantify the swirling features. Strong swirl (i.e., $S > S_{cr} \approx 0.6$) leads both to the Vortex Breakdown Bubble (VBB) and the formation of a Central Recirculation Zone (CRZ), which is especially efficient both in improving fuel-air mixing and

Salvador, F.J., Carreres, M., García-Tíscar, J., Belmar-Gil, M., "Modal decomposition of the unsteady non-reactive flow field in a swirl-stabilized combustor operated by a Lean Premixed injection system", Aerospace Science and Technology 112:106622 (author version).

doi: 10.1016/j.ast.2021.106622

in stabilising flames. Nevertheless, this also induces undesired effects in practical applications since the system becomes less receptive to external control, increasing pressure drops in non-reacting flows and combustion instabilities with an eventual local flame quenching in reacting applications due to the appearance of a Precessing Vortex Core (PVC). The PVC is characterised by the precession of the swirling jet around its axis and usually appears after the onset of the vortex breakdown. Such phenomena are strongly unsteady and three-dimensional, being complex to study experimentally and even numerically. In this context, advanced statistical data processing techniques based on linear-algebra tools such as the Proper Orthogonal Decomposition (POD) [7] and the Dynamic Mode Decomposition (DMD) [8] have emerged in the recent past with the aim of shedding some light on the flow diagnostics to characterise their structure and extract complementary information.

These two powerful tools complement each other and have been applied to extract the low-order coherent structures acting as precursors of the global self-sustained oscillations. On the one hand, the POD technique serves to identify the modes that represent the highest energy content through spatial correlations of a given flow field variable. Even though the statistical analysis of flow fields using POD has been established as a valuable tool for the characterisation of coherent vortex structures, it is not well-considered for reacting flows since its decomposition technique does not account for density variations. On the other hand, the DMD technique allows detecting in a more precise (less biased) way both the frequencies and the stability eigenmodes of the flow field through the extraction of spatial modal (low-dimensional coherent) structures and their corresponding growth/decay rates.

Lumley [9] was the first to use the Proper Orthogonal Decomposition (POD) technique to track the behaviour of coherent structures in turbulent flows. From then on, POD has been extensively used to analyse many different complex flows. In the reciprocating ICE field, POD has been applied to analyse issues such as acoustic impact and spark-ignition misfire both experimentally [10-16] and numerically [17, 18], and more recently to study pressure resonance phenomena [19] through CFD simulations. Meanwhile, in aeronautical research, POD has demonstrated to be useful for multiple applications such as the analysis of the aircraft engine noise [20-22], and the optimisation of compressors [23, 24] and turbines [25], being also able to identify from external aerodynamic fluctuations [26] to wing aeroelastic responses [27]. Specifically, aeroengine combustors have been experimentally investigated through POD decomposition techniques. Based on the PIV measurements, the presence of the Vortex Breakdown and the precession of the vortex core have been partially revealed and characterised in strongly swirling jets using modal decomposition analysis both in non reactive [28-34] and reactive [35-37] conditions. Nevertheless, as a consequence of experimental diagnosis shortcomings (e.g.,

Salvador, F.J., Carreres, M., García-Tíscar, J., Belmar-Gil, M., "Modal decomposition of the unsteady non-reactive flow field in a swirl-stabilized combustor operated by a Lean Premixed injection system", Aerospace Science and Technology 112:106622 (author version).

doi: 10.1016/j.ast.2021.106622

sampling frequency of the Stereo PIV system can be sometimes much smaller than the PVC frequency [30]), temporal- and spatial-detailed CFD simulations have emerged as a potential tool to successfully characterise the coherent structures within the combustor through pressure, vorticity and species signals decomposition rather than dealing just with velocity. In this way, the POD technique applied to numerical studies has characterised the Vortex Breakdown Bubble and the transition to helical breakdown modes in non-reacting conditions [38, 39], the combustion dynamics and flame interactions in reactive conditions [40-43], and the impact of variations of thermal load and global equivalence ratio on combustion acoustics noise levels [44].

On the other hand, the Dynamic Mode Decomposition technique [8] has been used in recent turbulent flow investigations [45, 46]. So far, this post-processing tool has been limitedly employed for simple modal flow decomposition in reciprocating engines [18, 19]. In fact, even in gas turbine research, its application to the combustion problem is still scarce, focused on experimental PIV data analysis based on velocity and vorticity fields [47], Schlieren jet flow [48] and shear layer flow [49] measurements. It has been only in the very recent years when DMD has been successfully applied both to experimental aero-engine investigations, such as cavity flows [50], fan [51] and combustion [52-53] noise, and to CFD studies to a lesser extent (e.g., radial [24] and centrifugal [54] compressors, and swirled-stabilised lean combustors [55]), where DMD has allowed obtaining flame structures and dominant acoustic modes.

The present work reports on a detailed numerical study of the low-dimensional dynamics of the pressure and velocity field evolution in a gaseous-fueled swirled-stabilised academical combustor in non-reacting conditions for which detailed measurements are available [56]. The primary motivation of this study is to develop systematic advanced mathematical procedures for the analysis of complex data sets used for comparison, validation and identification of physical mechanisms. Precisely, POD and DMD modal post-processing decomposition techniques are applied to a Dynamic Smagorinsky Large Eddy Simulation CFD model of an academic combustor operated by a Lean Premixed (LP) injection system. The predictive capability of the model has been previously validated to reveal the unsteady behaviour of flow field features in the chamber and its complex interactions with the geometry. This work constitutes the first attempt to apply and compare POD and DMD techniques to the studied non-reacting test case. The non-reacting flow is known to be a crucial step in LDI combustor research since the success or failure of ignition (and re-ignition at high-altitude) is known to directly depend on local conditions just before ignition, especially on the mixture quality and the turbulence level at the near-injection region. Aditionally, by first considering a non-reacting case, the objective is to isolate the flow-dynamics solely related to the injection, decoupling the resulting modes and features from those related to combustion.

Salvador, F.J., Carreres, M., García-Tíscar, J., Belmar-Gil, M., "Modal decomposition of the unsteady non-reactive flow field in a swirl-stabilized combustor operated by a Lean Premixed injection system", Aerospace Science and Technology 112:106622 (author version).

doi: 10.1016/j.ast.2021.106622

In addition, the reduced complexity when compared to a reacting case is helpful to define and validate the implementation of the data-driven modal decomposition techniques.

The application of these decomposition methods allows extracting the most energetic 3D spatial modes and reveal how to promote particular modes that may be of interest for the mixing process or, in reverse, how to weaken or even eliminate modes that may be harmful (e.g., in case their main frequency as identified by the decomposition techniques is close to a resonance frequency of the chamber, the turbine blades downstream, etc.). In addition, identifying the frequencies of the different modes can allow geometric modifications that redistribute the acoustic energy to a more convenient frequency band, for instance one that is already masked by other noise sources such as the compressor or the jet mixing process.

The remainder of the paper is organised as follows. In **Section 2**, an overview of the mathematical models of POD and DMD techniques is presented. **Section 3** describes the model combustor, spatial discretisation of the computational domain, and imposed boundary conditions. Furthermore, the model validation of the LES simulation is here reported together with the data preparation for decomposition. **Section 4** discusses the simulation outcomes, first in terms of predicted flow topology features, and then the POD and DMD decomposition results. Finally, the conclusions of the study, including a summary of the comparisons between POD and DMD, are given in **Section 5**.

## 2. DATA ANALYSIS TECHNIQUES

The Proper Orthogonal Decomposition (POD) and Dynamic Mode Decomposition (DMD) methods of ensembles of the instantaneous pressure and velocity fields are employed to obtain a deeper insight into the time-spatial modal characteristics of the unsteady coherent flow structures. Both techniques transform the pressure and velocity fields in a finite series of products of spatial functions with time-dependant coefficients.

### 2.1. Proper Orthogonal Decomposition

The Proper Orthogonal Decomposition (POD) technique, also called Principal Component Analysis (PCA) consists in the flow decomposition into coupled spatial and temporal orthogonal modes. In this way, the spatial structures comprising most of the flow field energy are identified through the ordering of the contribution of each mode. Please note that the full flow field can be reconstructed through the superposition of all modes.

The evolution of the flow field in CFD simulations is usually presented in a sequence of $N$ temporal snapshots ($\boldsymbol{v}_i$), gathered in a matrix $\boldsymbol{V}$:

Salvador, F.J., Carreres, M., García-Tíscar, J., Belmar-Gil, M., "Modal decomposition of the unsteady non-reactive flow field in a swirl-stabilized combustor operated by a Lean Premixed injection system", Aerospace Science and Technology 112:106622 (author version).

doi: 10.1016/j.ast.2021.106622

$$\boldsymbol{V}_1^N = \{\boldsymbol{v}_1, \boldsymbol{v}_2, \dots, \boldsymbol{v}_N\} \quad (1)$$

These snapshots should be separated by a constant time step ($\Delta t_{POD}$) and usually contain a quantity M of scalar flow magnitudes such as velocity and vorticity components, density, pressure, or species.

POD can then be performed by solving the associated eigensystem of the diagonalised time-averaged correlation matrix $\boldsymbol{V}^T\boldsymbol{V}$ [8]. Nevertheless, since $\boldsymbol{V}^T\boldsymbol{V}$ resolution can be computationally expensive ($N \times N$ matrix) an alternative approach based on the Singular Value Decomposition (SVD) of $\boldsymbol{V}$ [57] is generally preferred:

$$\boldsymbol{V} = \boldsymbol{U}\boldsymbol{\Sigma}\boldsymbol{W}^T \quad (2)$$

Here, the columns of $\boldsymbol{U}$ ($M \times N$ matrix) correspond to the left-singular vectors known as POD spatial modes $\boldsymbol{\psi_i}$, which form an orthonormal basis of $\boldsymbol{V}$. Note that the validity of this alternate approach is proved since the spatial modes are also the eigenvectors of $\boldsymbol{V}^T\boldsymbol{V}$. Next, $\boldsymbol{\Sigma}$ is a diagonal matrix of dimensions $M \times N$ whose non-zero elements correspond to the squared eigenvalues of $\boldsymbol{V}^T\boldsymbol{V}$ (usually called singular values) and thus represents the contribution of each spatial mode $\boldsymbol{\psi_i}$ to the total energy of matrix $\boldsymbol{V}$, defined by Nikiforov [58] as the sum of all singular values. Finally, $\boldsymbol{W}$ corresponds to the right-singular vectors of $\boldsymbol{V}$, being the temporal evolution $a_i(t)$ of each spatial mode $\boldsymbol{\psi_i}$ described by the rows of $\boldsymbol{\Sigma W^T}$. Therefore, the overall flow field can be understood as a linear superposition of spatial and temporal data:

$$\boldsymbol{V}(\boldsymbol{x}, t) = \sum_{i=1}^{N} \boldsymbol{\psi_i}(\boldsymbol{x})\, \boldsymbol{a_i}(t) \quad (3)$$

The main interest of the POD technique is the possibility of dimensionality reduction, crucial in CFD simulations where output data is arranged in big matrices. In this way, the total flow field can be reconstructed by applying Eq. 3 taking into account a reduced number of modes $L$ and ensuring that the reconstructed flow field $\widetilde{\boldsymbol{V}}$ is the closest to the original by the minimisation of the Frobenius norm.

### 2.2. Dynamic Mode Decomposition

The Dynamic Mode Decomposition (DMD) technique aims at grouping coherent spatial features into modes (eigenvectors) of a single temporal frequency, allowing the identification of coherent but weakly-energetic modes in highly transient regimes. Recalling the matrix $\boldsymbol{V}_1^N$ introduced in **Section 2.1**, containing $N$ snapshots of the flow field, and assuming these to be linearly correlated through an unknown matrix $\boldsymbol{A}$, which in turn remains almost constant during the time $N \cdot \Delta t_{DMD}$ spanned by Eq. (4):

$$\boldsymbol{v_{i+1}} = \boldsymbol{A}\boldsymbol{v_i} \quad (4)$$

Then, the evolution and dynamic characteristics of the flow field can be characterised by the eigenvalues (i.e., DMD

Salvador, F.J., Carreres, M., García-Tíscar, J., Belmar-Gil, M., "Modal decomposition of the unsteady non-reactive flow field in a swirl-stabilized combustor operated by a Lean Premixed injection system", Aerospace Science and Technology 112:106622 (author version).

doi: 10.1016/j.ast.2021.106622

eigenvalues) and eigenvectors (i.e., DMD modes) of this matrix. It should be clear that even if the flow field is non-linear, matrix $\boldsymbol{A}$ provides a linear approximation of the flow evolution. Eq. (1) and Eq. (4) can be combined in matrix form:

$$\boldsymbol{V}_2^N = \boldsymbol{A}\boldsymbol{V}_1^{N-1} \tag{5}$$

The eigendecomposition of $\boldsymbol{A}$ is usually too computationally expensive to be performed directly. Thus, Singular Value Decomposition (SVD) can be used again as in Section 2.1 in order to obtain $\boldsymbol{V}_1^{N-1} = \boldsymbol{U}\boldsymbol{\Sigma}\boldsymbol{W}^T$, then reformulating Eq. 5 as:

$$\boldsymbol{V}_2^N = \boldsymbol{A}\boldsymbol{U}\boldsymbol{\Sigma}\boldsymbol{W}^T \tag{6}$$

Now, a new matrix $\tilde{\boldsymbol{S}}$ can be built through the manipulation of terms that are already known. The matrix $\tilde{\boldsymbol{S}}$ is constructed ensuring *matrix similarity* with **A**:

$$\tilde{\boldsymbol{S}} \triangleq \boldsymbol{U}^T\boldsymbol{V}_2^N\boldsymbol{W}\boldsymbol{\Sigma}^{-1} = \boldsymbol{U}^T\boldsymbol{A}\boldsymbol{U} \tag{7}$$

Because of this similarity, the eigenvalues $\lambda_i$ of $\tilde{\boldsymbol{S}}$ match those of **A**, with the advantage that $\tilde{\boldsymbol{S}}$ is of reduced size and easier to solve. Then, the DMD modes $\Phi_i$ can be computed by mapping the eigenvectors $y_i$ (eigenvector matrix $\boldsymbol{Y}$) of $\tilde{\boldsymbol{S}}$ into the non-reduced space through $\boldsymbol{U}$ (note that $\boldsymbol{U}$ is the POD basis of $\boldsymbol{V}_1^{N-1}$):

$$\boldsymbol{\Phi} = \boldsymbol{U}\boldsymbol{Y} \tag{8}$$

Since the numerical routine implemented in the present investigation normalise the calculated eigenvectors, it is necessary to recover the modal amplitudes $\alpha_i$. This can be easily done by solving the reconstructed flow field multiplied by the unknown amplitudes against any snapshot of the flow [59]:

$$\boldsymbol{V}_1 = \boldsymbol{\Phi}\boldsymbol{\alpha} \Rightarrow \boldsymbol{\alpha} = \boldsymbol{\Phi}^{-1}\boldsymbol{V}_1 = \boldsymbol{Y}^{-1}\boldsymbol{U}^*\boldsymbol{V}_1 \tag{9}$$

Please note that $\boldsymbol{U}$ is unitary and thus its conjugate transpose $\boldsymbol{U}^*$ is also its inverse. Now the system can be solved inverting $\boldsymbol{Y}$ rather than the higher-order $\boldsymbol{\Phi}$. In this way, the full dynamics of the flow field, represented by the snapshot matrix at discrete time steps $t_k$, can be reconstructed by the linear superposition of the DMD modes:

$$\boldsymbol{V}(\boldsymbol{x}, t_k) = \Re\left\{\sum_{i=1}^{N-1} \boldsymbol{\Phi}_{\boldsymbol{i}}(\boldsymbol{x})\alpha_i\lambda_i^{k-1}\right\} = \Re\{\boldsymbol{\Phi}\boldsymbol{D}_{\boldsymbol{iag}}(\boldsymbol{\alpha})\boldsymbol{V}_{\boldsymbol{and}}(\boldsymbol{\lambda})\} \tag{10}$$

Where $\boldsymbol{D}_{\boldsymbol{iag}}(\boldsymbol{\alpha})$ is the diagonal matrix of modal amplitudes, and $\boldsymbol{V}_{\boldsymbol{and}}(\boldsymbol{\lambda})$ is the Vandermonde matrix of the eigenvalues. Furthermore, the single frequency ($f_i$) associated to each DMD mode can be recovered considering the time step ($\Delta t_{DMD}$) between snapshots:

$$f_i = \frac{\omega_i}{2\pi} = \frac{\Im\{\ln(\lambda_i)\}}{2\pi\Delta t_{DMD}} \tag{11}$$

Finally, the calculated DMD modes need to be ranked in relevance. To do so, Kou & Zhang [60] have recently proposed



doi: 10.1016/j.ast.2021.106622

a simple criterion that considers the evolution of each dynamic mode within the whole sampling space, and ranks them according to their contribution to all samples:

$$E_i = \sum_{j=1}^{N} \left|\alpha_i \lambda_i^{j-1}\right| \|\boldsymbol{\Phi_i}\|_F^2 \, \Delta t_{DMD} \tag{12}$$

## 3. COMPUTATIONAL SETUP AND METHODOLOGY

### 3.1. Computational domain

The computational investigation has been carried out based on the experimental gaseous configuration of the CORIA academical combustor [56], whose 3D model is depicted in **Figure 1**. This burner configuration contains four major components: a plenum to tranquillize the flow before entering the swirler, a radial-swirl injection system, a square cross-section combustion chamber (100x100x260 mm) and a convergent exhaust to prevent air recirculation. The combustor employs a radial swirler, composed of 18 channels inclined at 45º with an external diameter of $D$ = 20 mm. The swirler creates a swirling air flow in the combustion chamber, in which gaseous methane is injected through a tube ($d$ = 4 mm) acting as fuel injector located in the centre of the swirler.

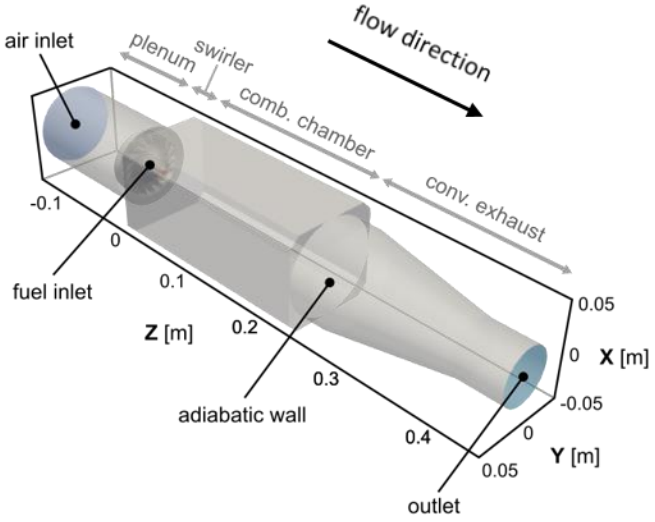


Figure 1. Global view of the CORIA single burner computational domain.

In this work, a premixed gaseous injection strategy has been simulated at ambient conditions ($T$ = 298 K; $p$ = 1 atm), for which detailed measurements are available [56]. The operating condition corresponds to a global equivalence ratio of 0.75, where the swirler and the central jet are fed with 5.612 g/s and 0.236 g/s of a fully mixed air-methane mixture,

Salvador, F.J., Carreres, M., García-Tíscar, J., Belmar-Gil, M., "Modal decomposition of the unsteady non-reactive flow field in a swirl-stabilized combustor operated by a Lean Premixed injection system", Aerospace Science and Technology 112:106622 (author version).

doi: 10.1016/j.ast.2021.106622

respectively. Meanwhile, an inlet flow velocity of 28.8 m/s gives rise to a Reynolds mean number of 35,000 based on the mean diameter of the convergent inlet.

### 3.2. Numerical Setup

The Large Eddy Simulation reported in this paper is performed with the commercial code CONVERGE™ [61], which allows using simple orthogonal grids and automates the mesh generation process. A second-order-accurate (upwind) spatial discretization scheme is used for the governing conservation equations, while a second-order (upwind) implicit formulation is set for time discretization. Meanwhile, the transport equations are solved using the PISO algorithm. A variable time-stepping algorithm is used in the current investigation, where the time-step is automatically calculated each computational cycle, ensuring that the maximum CFL-number does not exceed 0.8 anywhere in the computational domain at any instant [61]. This results in time steps in the order of 1 to 2 μs. The Dynamic Smagorinsky LES sub-grid scale model has been chosen for the treatment of turbulence to characterize the unsteady non-reacting flow field.

The meshing strategy here employed is selected from a previous work where the authors defined a methodology to derive a mesh as a compromise between spatial resolution and computational cost in order to work out this multi-scale problem [62]. In this regard, the three-dimensional domain is discretized in a structured grid of hexahedrons with a base cell size of 2 mm. To ensure an accurate prediction of the flow behavior, the cell size is reduced in areas where a finer resolution is critical to the accuracy of the solution (i.e., the flow behavior within the small passages of the swirler), by applying a grid-scale factor ($r$), according to:

$$L_{scaled} = \frac{L_{base}}{2^r} \tag{13}$$

Following the conclusions extracted in the mentioned mesh methodology, a scale factor of three is applied as fixed embedding to the swirler and combustion chamber entrance. Additionally, another scale factor of three is applied in the adaptive mesh refinement algorithm (AMR), both to increase the spatial resolution where velocity gradients are significant and to maintain the proper level of mesh near the wall (see **Figure 2**). In this way, $y^+$ values between 30 and 100 have been ensured, the Werner and Wengle wall model being then used to determine the tangential components of the stress tensor at the wall. The total number of cells depends on the simulation timing and varies among 15 and 17 million.

Salvador, F.J., Carreres, M., García-Tíscar, J., Belmar-Gil, M., "Modal decomposition of the unsteady non-reactive flow field in a swirl-stabilized combustor operated by a Lean Premixed injection system", Aerospace Science and Technology 112:106622 (author version).

doi: 10.1016/j.ast.2021.106622

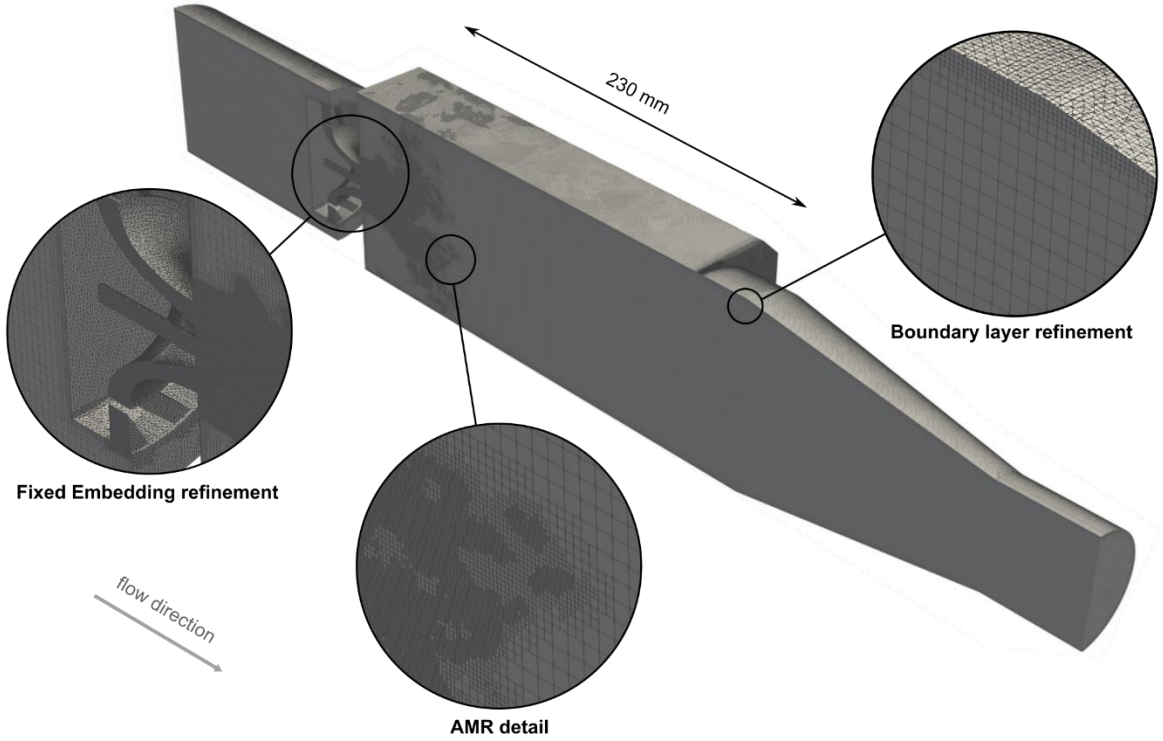


Figure 2. Computational mesh illustrating the strategy considered, consisting in 3 levels of fixed embedding, 3 levels of AMR, and 2 layers with 2 levels of wall refinement.

A mesh scaling of twice the baseline mesh size was used to stabilize the flow field for a given time before automatically scaling down to the base mesh size and starting the usage of fixed embedding and AMR tools. This time has been chosen as 25 rotations of the large coherent structures generated within the combustor ($\tau = \tau_{PVC} \approx 2$ ms, see **Section 4.1**), i.e. $|t/\tau| = 25$ (50 ms of physical time). The simulation was run for an additional time of $|t/\tau| = 50$ (100 ms) to stabilize the overall mass flow rate and the velocity fields with the final mesh strategy. From this point, hereinafter treated as the origin of times ($t/\tau = 0$) turbulent statistical averages and higher-order moments started being calculated ($t/\tau \geq 0$). Statistics were computed from $t/\tau = 0$ to $t/\tau = 50$ (i.e., for 100 ms). The overall computational cost of the simulation (from $t/\tau = -75$ to $t/\tau = 50$) is about 35k CPU hours and 300 GB of RAM memory.

### 3.3. Model Validation

Before applying the modal decomposition techniques, the accuracy of the LES prediction was evaluated by comparing the mean and fluctuating velocity profiles to experimental data available for 5 radial stations ($x$ = 0 corresponds to the centerline of the chamber) located downstream of the swirler exit. As an example, **Figure 3** shows the radial distributions of the mean axial and tangential velocity components and their root-mean-square (representing the turbulent velocity or fluctuations), at five axial locations ($z$ = 5, 10, 20, 30 and 40 mm) within the CORIA burner.

Salvador, F.J., Carreres, M., García-Tíscar, J., Belmar-Gil, M., "Modal decomposition of the unsteady non-reactive flow field in a swirl-stabilized combustor operated by a Lean Premixed injection system", Aerospace Science and Technology 112:106622 (author version).

doi: 10.1016/j.ast.2021.106622

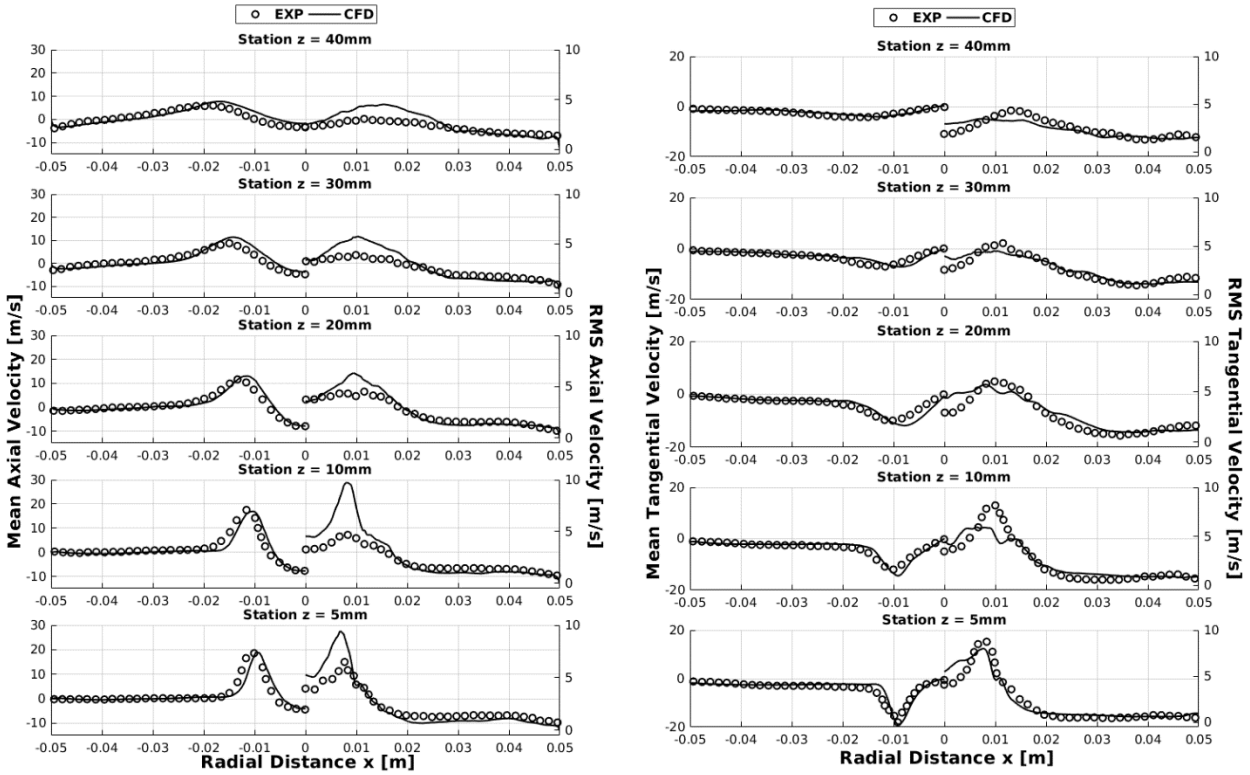


Figure 3. Mean and RMS Axial (a) and Tangential (b) velocity profiles obtained from LES at five axial locations.

At a first glance, the global flow topology and the amplitude of the mean and RMS velocity profiles are well reproduced. The mean velocity profiles (left side of **Figures 3(a)** and **3(b)**) obtained from the CFD code show that the computed velocity field is, qualitatively, in good agreement with experiments throughout the five stations and the LES seems to accurately capture the jet opening angle, denoted by the peaks of the mean velocity components around $x$ = 10 mm. Moreover, the high mean tangential velocity values observed on the left side of **Figure 3(b)** confirm the strong swirl number of the injection system at the injection plane, reaching values as high as those obtained for the axial component. This leads to the formation Vortex Breakdown Bubble (VBB) and thus to the generation of a Central Recirculation Zone (CRZ). On the other hand, the turbulent velocity, given by the root mean square value (i.e., the RMS depicted on the right side of the figures), is slightly over-predicted. This could be partly attributed to the fact that the PIV resolution used for measurements is 1 mm [56], which is larger than the LES filter size in the near-injection zone, resulting in smaller measured RMS values due to averaging effect within the probe. For a complete model validation and LES quality assessment, please refer to a previous work by the authors [62].

### 3.4. Data preparation for decomposition

In order to apply the modal decomposition procedures presented in **Section 2**, the instantaneous pressure field is exported



doi: 10.1016/j.ast.2021.106622

to text files containing the cell centroid coordinates [**x y z**] and its corresponding static pressures **p**. For this analysis, a total of 200 snapshots are gathered during a simulated physical time of 20 $\tau$ (from $t/\tau = 30$ to $t/\tau = 50$), which implies a spectral resolution of 33.3 Hz. Data are then exported every 0.1 ms (±1 μs due to the variable time-stepping algorithm), corresponding to 50-100 simulation time steps. This implies obtaining a sampling frequency of 10 kHz, which is enough to apply the Nyquist criterion in order to isolate the relevant information. This allows optimizing both the processing computational cost and storage space.

However, since the adaptive mesh refinement algorithm is continuously modifying the number of cells, the spatial coordinates of each exported snapshot do not remain constant. Therefore, the raw data require some preliminary treatment as the decomposition techniques require constant spatial coordinates. In this previous step, a subset of 1 million random cells (preventing any user-induced biasing) is selected from the first snapshot and taken as spatial reference. A sensitivity study performed by the authors suggested the size of the subset provides an adequate compromise between computational cost and spatial resolution.

The procedure to relate the coordinates of the cell centroids of subsequent snapshots (which will have changed due to the AMR, as stated) is to identify the nearest neighbour of each of the reference coordinates. To do so, a *k-d* tree data structure [63] is generated in order to organize the raw coordinates from each new snapshot. Then, a searcher algorithm [64] computes both the indices of the new snapshot cells that best match the reference coordinates and the Euclidean $d_i$ between them. A validation is performed to discard cells whose computed distance $d_i$ to their corresponding reference is greater than 1mm, thus ensuring spatial consistency. Hence, only the pressure and velocity values of the suitable cells of a given snapshot are stored in the corresponding vector $\boldsymbol{v_i}$ defined in **Section 2**. Finally, once the snapshot matrix $\boldsymbol{V}$ is assembled, rows with "NaN" values (from cells that failed the validation) are discarded, thus obtaining a suitable matrix of consistent and continuous pressure and velocity values at nearly constant spatial locations.

## 4. RESULTS AND DISCUSSION

### 4.1. Flow Morphology

A preliminary analysis of the raw pressure and velocity fields is carried out to characterize the swirling flow dynamics and to assess the presence of time-evolving structures within the combustor. The generation of unsteady coherent structures depends mainly on the swirl intensity, defined by the swirl number $S_W$, which can be expressed according to Eq. (13) [65]:



doi: 10.1016/j.ast.2021.106622

$$S_w = \frac{1}{R_{ext}} \frac{\int_0^{R_{ext}} \rho u_z u_\theta r^2 dr}{\int_0^{R_{ext}} \rho u_z^2 r dr} \tag{13}$$

When $S_W$ exceeds a critical value in the swirler outlet region (typically 0.6 in such flows [42]), a phenomenon known as Vortex Breakdown Bubble (VBB) occurs, leading to the formation of a Central Recirculation Zone (CRZ) encompassed by the inner mixing shear layer. In the present work, the swirl number evaluated in the injection plane of the combustion chamber is 0.76 [56], implying that the formation of a VBB is expected. The VBB can be described as the formation of a free stagnation point and a recirculation zone with a surrounding 3D spiral flow in the core.

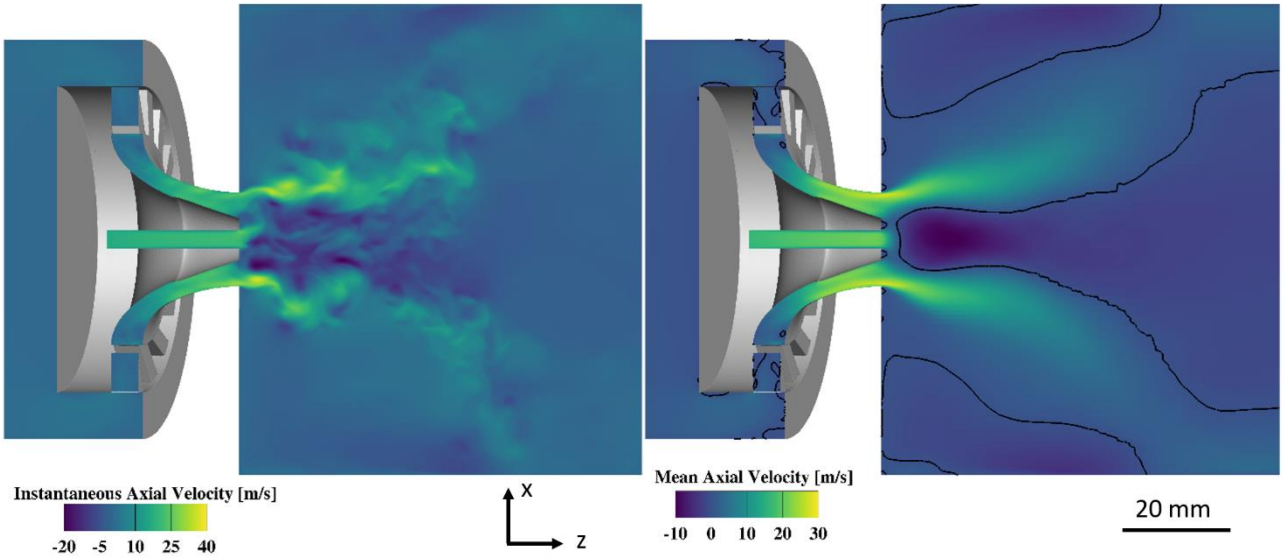


Figure 4. Contours of instantaneous (a) and time-averaged (b) axial velocity at $t/\tau = 27$ in a central cut of the CORIA burner.

**Figure 4(a)** shows the contour of the instantaneous axial velocity field at $t/\tau = 27$, whereas **Figure 4(b)** depicts the time-averaged axial velocity field. Even though the recirculation zones shown in **Figure 4(b)** may appear to be confined regions with well-defined boundaries (zero-axial velocity regions are highlighted in black) the instantaneous flow field is much more dynamic and complex. The time-averaged axial velocity field hides the highly unsteady local assymetry, turbulent mixing, and interactions that take place in this region. The boundary of the CTRZ is barely seen in the instantaneous field, which shows smaller and isolated recirculation zones with a high degree of unsteadiness. Furthermore, the contours show that the LES grid can resolve a large extent of small-scale turbulent structures.

When the central vortex core starts precessing around the combustor axis of symmetry at a given frequency ($f_{PVC}$), it produces hydrodynamic instabilities. The frequency of precession is a function of the combustor design and the swirl

Salvador, F.J., Carreres, M., García-Tíscar, J., Belmar-Gil, M., "Modal decomposition of the unsteady non-reactive flow field in a swirl-stabilized combustor operated by a Lean Premixed injection system", Aerospace Science and Technology 112:106622 (author version).

doi: 10.1016/j.ast.2021.106622

intensity at the inlet. This unstable mode, typically related to the VBB, can be defined as the Precessing Vortex Core (PVC), and it is usually located along the outer boundary of the CRZ. Further downstream of the injection position, turbulence breaks this large vortical structure into small scale ones, no coherent PVC being detected.

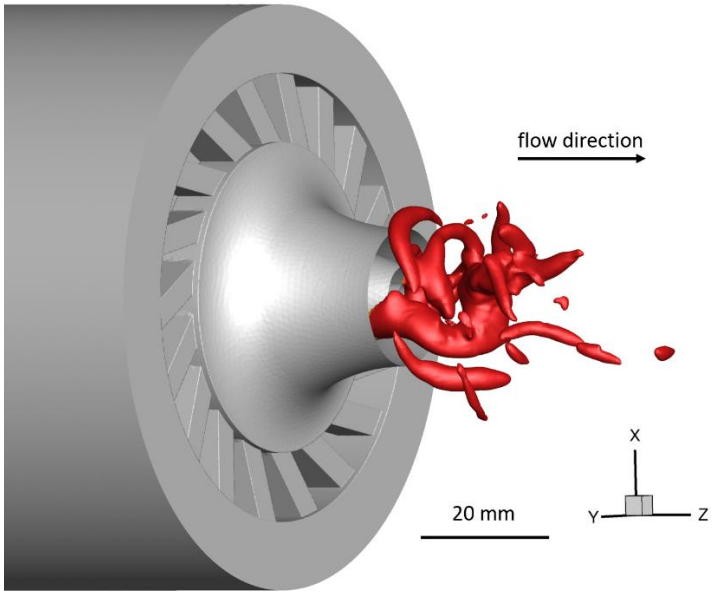


Figure 5. Instantaneous visualization of the Precessing Vortex Core identified through a pressure iso-surface of the instantaneous pressure $\bar{p} = 101.1$ kPa at $t/\tau = 25$.

The structure of the PVC generated within the combustor is well captured by LES and visualized in **Figure 5** through an iso-surface of the unsteady pressure field. The PVC presents an asymmetric shape around the central axis and tends to align with it near the inlet. However, when it reaches the stagnation point, it forms a spiral pattern further downstream in the axial direction. The image exhibits two rotating helicoidal branches ejected from inside the swirler entering the chamber and being reoriented by the mean rotating flow. The swirling motion induces a centrifugal force that drives the large and coherent vortical structures away from the central axis. These coherent structures are the primary source of unsteadiness in the swirler outlet region and have a substantial impact on flame propagation. In fact, the flame front can be affected by the highly turbulent aerodynamic stretching caused by the PVC, thus leading to local quenching or extinction.

The presence of instantaneous negative axial and tangential velocities in the region near the centerline of the combustion chamber can be directly attributed to the existence of the PVC. Meanwhile, a rotation time scale associated to the PVC can be defined to identify some unsteady flow structures, as shown in Eq. (14):

Salvador, F.J., Carreres, M., García-Tíscar, J., Belmar-Gil, M., "Modal decomposition of the unsteady non-reactive flow field in a swirl-stabilized combustor operated by a Lean Premixed injection system", Aerospace Science and Technology 112:106622 (author version).

doi: 10.1016/j.ast.2021.106622

$$\tau_{rot} = \frac{2\pi R_i}{u_{\theta,i}} \tag{14}$$

where $R_i$ is the mean radius of the convergent inlet and $u_\theta$ is the mean tangential velocity component in the inlet plane of the combustion chamber (see **Section 3.1** for geometric details). For the combustor here investigated, the rotation time scale evaluated though Eq. (8) at the combustion chamber inlet is around 2 ms.

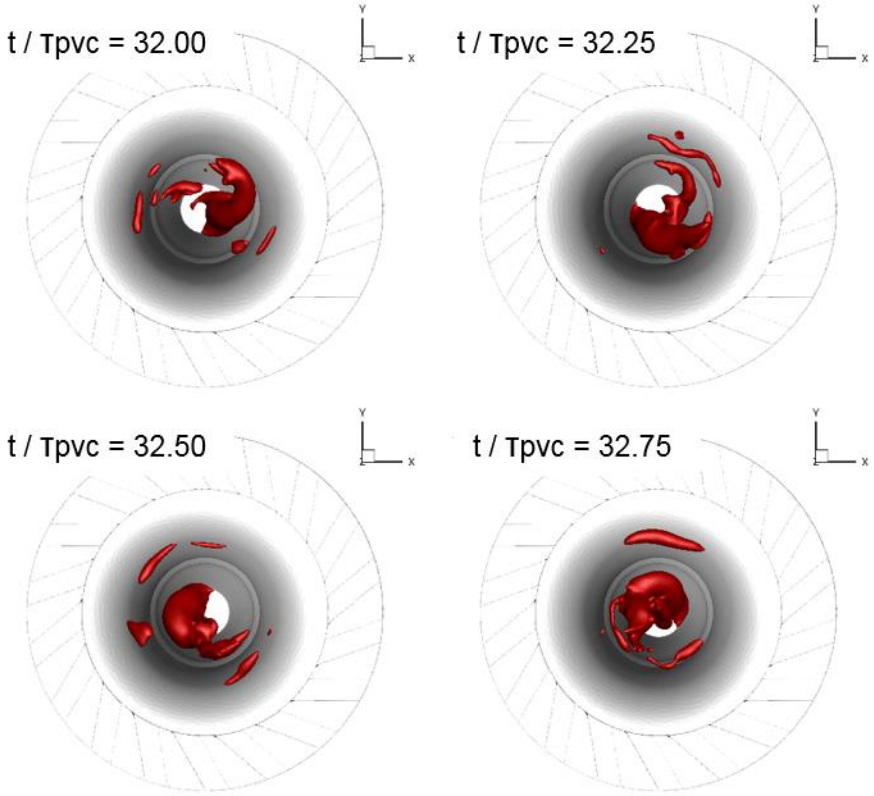


Figure 6. Time evolution of the PVC in one cycle of the precession motion. PVC is identified using an iso-surface of the instantaneous pressure $\bar{p} = 101.1$ kPa.

**Figure 6** presents four different snapshots to show the development of the so-called branches of the PVC within one cycle of the precession obtained from the LES. As can be noticed, the number of branches can vary with the course of time since just one helicoidal finger-like structure is now visualized. The turnover (or one complete rotation) time of this vortex structure is estimated at $\tau_{PVC}$ = 2.0 ms, close to the rotation time scale defined by Eq. (14), and corresponding to a precessing frequency of about $f_{PVC}$ = 500 Hz. The structure at $t/\tau_{PVC} = 32$ (considering an arbitrary absolute time after the flow stabilization as the start of a given rotation) is aligned to the central axis, but at $t/\tau_{PVC} = 32.25$ it is taken away from the core and turns in a spiral shape along the axial direction. The vortex spiral evolves from the shear layer due to Kelvin-Helmholtz instabilities in both the axial and azimuthal directions. Once the vortical structure has completed one



doi: 10.1016/j.ast.2021.106622

cycle, it is again driven towards the central axis and spreads outward rapidly breaking up into small-scale structures. These helical filaments present counterclockwise winding in space and clockwise rotation in time. Moreover, velocity vectors around the PVC showed clockwise rotation all along the filament. Indeed, the outer edge was observed to have positive axial velocity, while the inner regions had reverse flow. This PVC motion afffects the flow evolution in the combustion chamber and improves turbulence intensity and mixing levels. However, at given conditions a probable resonant coupling with low-frequency acoustic oscillation in the chamber can exist. The behavior and incidence of the PVC is more complex in reactive cases, not studied in the present work.

### 4.2. POD decomposition

A spectral analysis of the 3D flow field pattern is performed to capture the dominant coherent structures and confirm the occurrence of PVC in the swirler outlet region. Proper Orthogonal Decomposition is applied as described in **Section 2** to obtain the orthonormal spatial modes $\psi_i$ (with their principal values $\sigma_i$) and their corresponding temporal evolution coefficients $\boldsymbol{a_i}$. The relevance of each mode is characterized by measuring their overall energy contribution (through the principal values) to the total energy of the snapshot matrix. As the mean pressure of the chamber is not substracted, the first POD mode $\psi_1$ is homogeneously distributed through the chamber, resulting in a singular value $\sigma_1$ that represents a high percentage of the matrix energy (please note that the mean pressure is around 100 kPa, and the acoustic fluctuations are small when compared to the mean component).

Since the main interest of this study lies on extracting the unsteady structures within the combustor, the first mode related to the mean homogeneous pressure can be ignored. In this way, the remaining pulsating energy distribution among the subsequent modes is shown in the Pareto chart of **Figure 7**. It can be seen that POD modes $\psi_2$ to $\psi_{17}$ gather approximately 40% of the remaining energy, with 20% being gathered just by modes $\psi_2$ to $\psi_6$. Meanwhile, modes $\psi_2$ to $\psi_{100}$ represent 80% of the remaining energy, with the rest of the modes ($\psi_{101\text{-}208}$) representing just 20% of the remaining energy.

Salvador, F.J., Carreres, M., García-Tíscar, J., Belmar-Gil, M., "Modal decomposition of the unsteady non-reactive flow field in a swirl-stabilized combustor operated by a Lean Premixed injection system", Aerospace Science and Technology 112:106622 (author version).

doi: 10.1016/j.ast.2021.106622

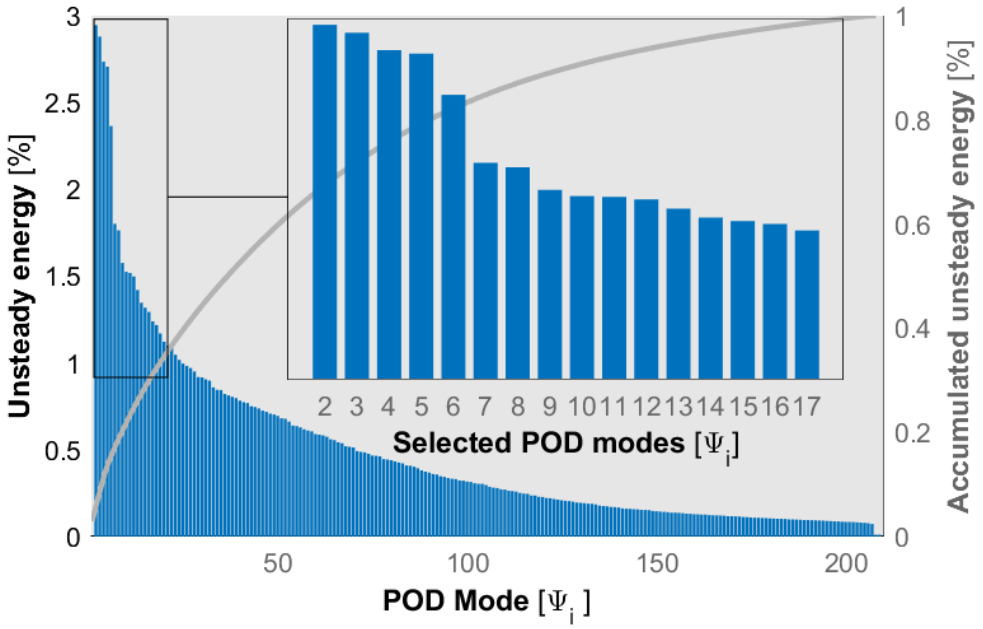


Figure 7. Pareto chart showing the singular values associated with POD modes $\psi_2$ to $\psi_{208}$ and accumulated contribution to the remaining energy after discarding the first mode related to the mean homogeneous pressure.

Besides the energy contribution of each mode, the analysis of its evolution in the frequency domain is carried out using the information contained within the time coefficients $\boldsymbol{a_i} = \sigma_i \boldsymbol{W_i^T}$. In this regard, **Figure 8** shows the amplitude of the POD modes in the frequency domain based on normalized periodograms of right-singular vectors $\boldsymbol{W_i^T}$. The strength of the energy of each spatial mode is shown through the Power Spectral Density (PSD) function of the time coefficient associated with its corresponding mode. The high energy content exhibited by modes $\psi_2$ to $\psi_6$ in **Figure 7** is here confirmed, and the spectral content of the higher-order modes (i.e., $\psi_7$ to $\psi_{17}$) appears nearly flat in comparison. It can also be seen how each of the most energetic POD modes ($\psi_2$ to $\psi_6$) only feature a well-defined frequency of interest, making it possible to attribute a specific phenomenon of known frequency to each mode when combined with the analysis of the spatial distribution of the modal energy. Nevertheless, higher-order modes ($\psi_7$ to $\psi_{17}$) present some kind of spectral mixing with several dominant frequencies ascribed to them. Furthermore, it is interesting to note how the two dominant frequency peaks (i.e., 526 Hz and 1053 Hz) seem to have two different POD modes with the same spectrum associated. This fact is consistent with the experimental measurements. (i.e., 507 Hz and 999 Hz, respectively) reported in the literature [66].

Salvador, F.J., Carreres, M., García-Tíscar, J., Belmar-Gil, M., "Modal decomposition of the unsteady non-reactive flow field in a swirl-stabilized combustor operated by a Lean Premixed injection system", Aerospace Science and Technology 112:106622 (author version).

doi: 10.1016/j.ast.2021.106622

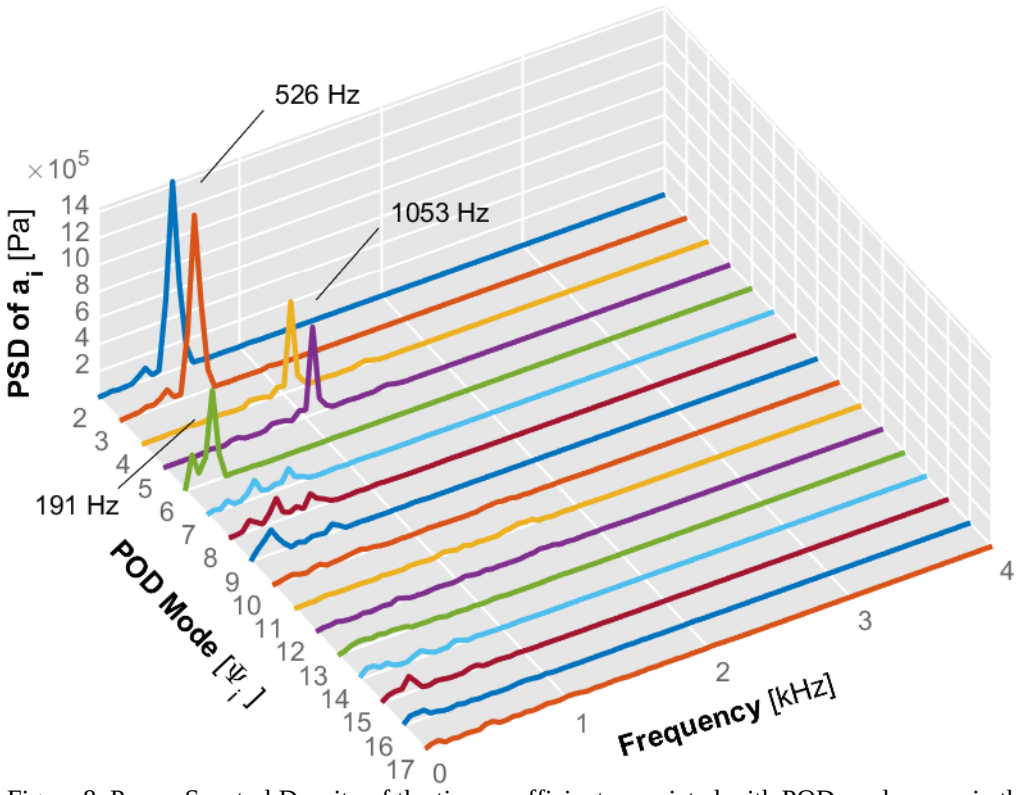


Figure 8. Power Spectral Density of the time coefficient associated with POD modes $\boldsymbol{\psi}_{2\text{-}17}$ in the frequency domain.

Finally, the spatial distribution of the POD modes can be visualized in **Figure 9** by plotting the values of the left-singular vectors $\boldsymbol{\psi_i}$ contained in the columns of $\boldsymbol{U}$ associated with each of the reference coordinates that were selected when building the snapshot matrix $\boldsymbol{V}$. The POD modes are represented through an iso-surface of the 5% (blue) and 95% (red) percentiles of the distribution of the real values of the mode $\Re\{\boldsymbol{\psi_i}\}$. In this way, the red and blue surfaces correspond to the opposite, most extreme values of the instantaneous pressure fluctuation, when reconstructed by multiplying the mode spatial amplitude $\boldsymbol{\psi_i}$ by the time evolution $a_i(t)$.

Salvador, F.J., Carreres, M., García-Tíscar, J., Belmar-Gil, M., "Modal decomposition of the unsteady non-reactive flow field in a swirl-stabilized combustor operated by a Lean Premixed injection system", Aerospace Science and Technology 112:106622 (author version).

doi: 10.1016/j.ast.2021.106622

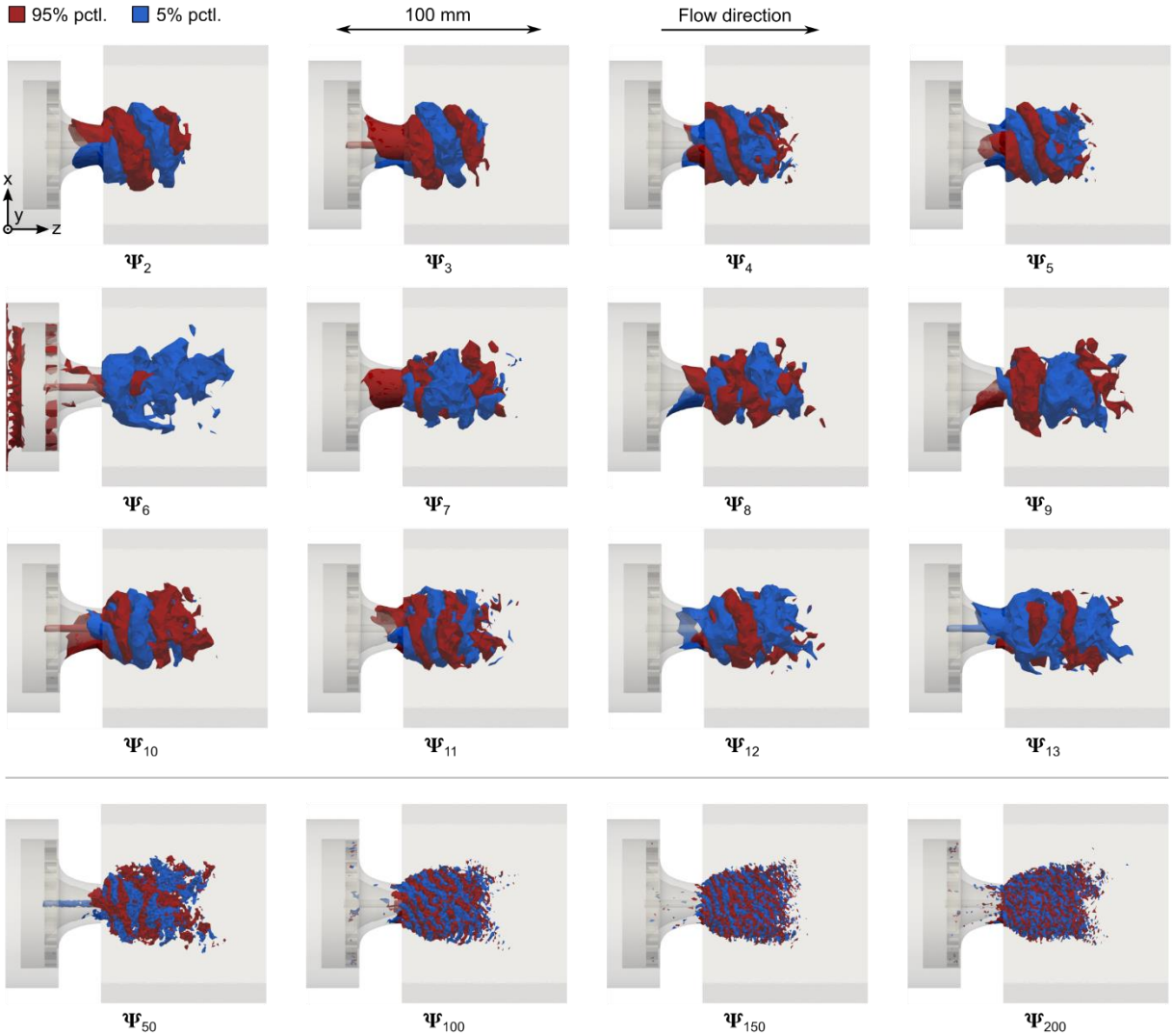


Figure 9. Spatial distribution of POD modes $\psi_{2\text{-}13}$ and $\psi_{50}$, $\psi_{100}$, $\psi_{150}$ and $\psi_{200}$ within the combustor.

Inspecting the shapes of modes $\psi_2$ and $\psi_3$ in **Figure 9**, it is clearly seen how the higher amplitudes are oscillating in opposite sides at the periphery of the CRZ. This single helical instability, born inside the swirler and reoriented by the mean rotating flow when entering the chamber, corresponds to the structure of the PVC defined in **Section 4.1**. In fact, the computed frequency of 526 Hz associated to these POD modes completely matches the precession frequency of the PVC, as estimated by Eq. (14) and represented in the time evolution of the PVC (see **Figure 6**). Please note that red and blue iso-surfaces correspond to a single structure where instantaneous pressure assumes strong positive and strong negative values separated by an angular distance of about π. Furthermore, these modes $\psi_2$ and $\psi_3$ resemble one another and are shifted in phase by π/2 (see **Figure 10**). As already observed by Oberleithnner et al. in a swirling jet facility

Salvador, F.J., Carreres, M., García-Tíscar, J., Belmar-Gil, M., "Modal decomposition of the unsteady non-reactive flow field in a swirl-stabilized combustor operated by a Lean Premixed injection system", Aerospace Science and Technology 112:106622 (author version).

doi: 10.1016/j.ast.2021.106622

composed by four tangential slots [29], this first pair of modes describes a travelling azimuthal wave with wavenumber $|m| = 1$ having a $\pi/2$ phase shift.

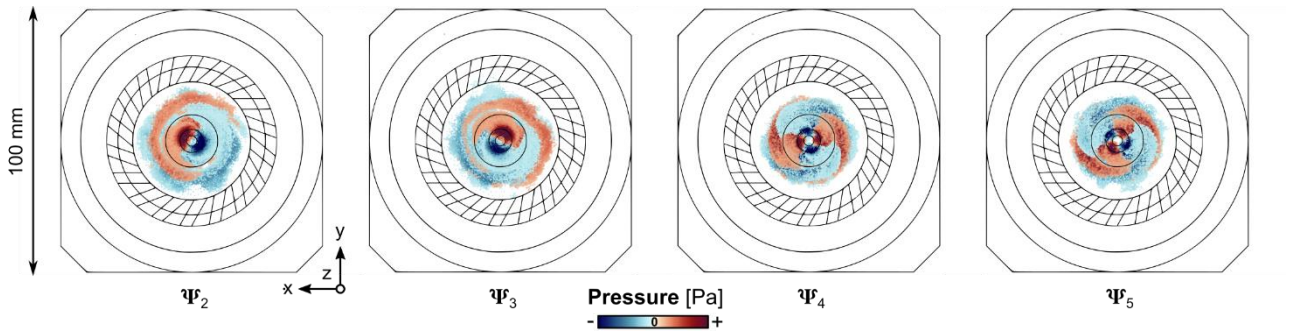


Figure 10. Frontal view of the spatial distribution of the first four POD modes $\psi_{2\text{-}5}$. Both mode pairs describe rotating structures with the same frequency with azimuthal wavenumber $|m| = 1$ for modes $\psi_2$ and $\psi_3$ and with $|m| = 2$ for modes $\psi_4$ and $\psi_5$.

The next two modes ($\psi_4$ and $\psi_5$) in **Figure 9** are interesting since their amplitudes are again predominantly gathered in the CRZ, but featuring a PVC with double spiral pattern structures and twice its rotating frequency ($f$ = 1053 Hz). These modes show a similar pattern to $\psi_2$ and $\psi_3$ but, in this case, characterized by the appearance of two vortices separated by an angular distance of about $\pi/2$. In such a case, the two modes seem rotated about $\pi/4$ with respect to each other, so that a travelling azimuthal wave with wavenumber $|m| = 2$ can be associated to them. The occurrence of this other coherent structure explains what was hinted in **Figures 5** and **6**, namely the intermittent emergence and disappearance of the branch-like structures of the PVC during the simulation. They describe coherent structures that are first growing and then decaying in the streamwise direction. Since the angles of the two pair of modes ($\psi_2$-$\psi_3$ and $\psi_4$-$\psi_5$) are in a ratio of about 2:1 and being the azimuthal periods of the waves $|m| = 1$ and $|m| = 2$ in the same ratio, it can be established that the two pairs of modes rotate at the same frequency and that the double helix (POD modes $\psi_4$ and $\psi_5$) is a harmonic of the single helix (POD modes $\psi_2$ and $\psi_3$).

In contrast with previous modes, the maximum amplitudes of $\psi_6$ are contained in a more uniform shape (see **Figure 9**). Moreover, the frequency content of this particular mode, peaking around 190 Hz (see **Figure 8**), is quite lower than the previous PVC modes. This spatial mode can be attributed to the generation of a well-defined CRZ since its period of around 5 ms is really close to the minimum amount of simulated time that the instantaneous axial velocity component needs to be time-averaged in order to identify the CRZ in the mean axial velocity field. Therefore, this axisymmetric fluctuation of the sixth mode of the flow is related to the axial displacement of the vortex breakdown location and is not correlated with the identified harmonic structures.

Salvador, F.J., Carreres, M., García-Tíscar, J., Belmar-Gil, M., "Modal decomposition of the unsteady non-reactive flow field in a swirl-stabilized combustor operated by a Lean Premixed injection system", Aerospace Science and Technology 112:106622 (author version).

doi: 10.1016/j.ast.2021.106622

Subsequent POD modes ($\psi_7 - \psi_{13}$) in **Figure 9** present a pattern of low-frequency and low-energy coupled effects. Since the flow is not entirely axisymmetric after passing through the 18 radial channels and emerging from the swirler, a high number of POD modes with similar but distorted shapes is expected as a consequence of the strong interaction among the unsteady PVC, the high turbulent CRZ and the strong shear layers. Finally, higher-order POD modes ($\psi_{50}$, $\psi_{100}$, $\psi_{150}$ and $\psi_{200}$) are represented to demonstrate the smaller size of these low-energetic structures and how, even so, they remain connected in a dominant spiral pattern, which might suggest potential acoustics coupling.

### 4.3. DMD decomposition

As previously introduced in **Section 2**, Dynamic Mode Decomposition is a well-suited tool for an in-depth frequency analysis since each mode is forced to contain a single frequency. Following the procedure outlined in the theoretical background, the relevance $E_i$ of each mode is computed considering the totality of the snapshots and then normalized with $E_i/max(\boldsymbol{E})$ to evaluate the relevance of the resulting DMD modes $\boldsymbol{\Phi_i}$. In this way, **Figure 11** shows a chart where DMD modes have been ordered according to their associated frequency and ranked using a normalized Kou & Zhangs's criterion [60], highlighting the eight most coherent modes at the frequencies of interest. Furthermore, the spatial distribution of the highly energetic flow regions pulsating at these different six mode frequencies can be visualized in **Figure 12**, following the same procedure used in the POD analysis.

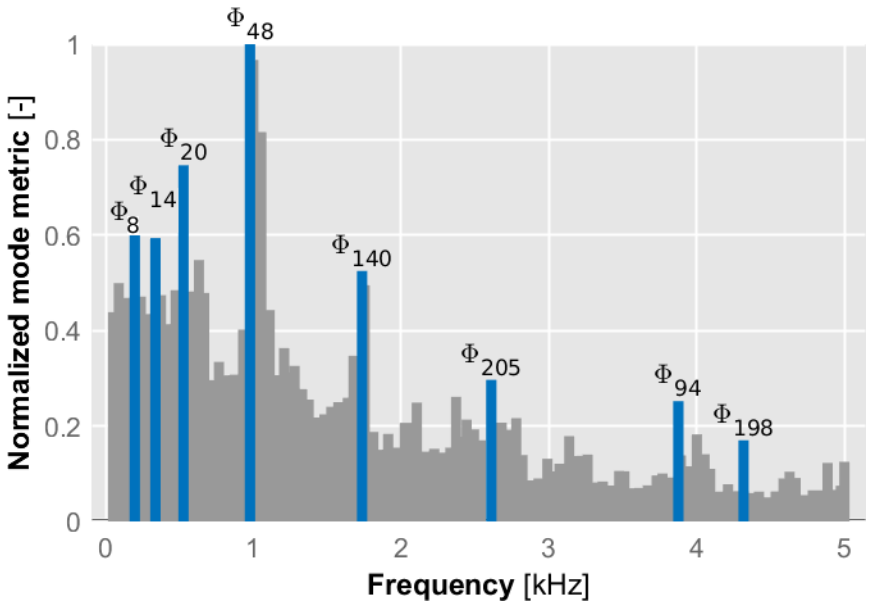


Figure 11. Normalized relevance $E_i/max(\boldsymbol{E})$ of the spectrum of DMD modes, highlighting the six most coherent modes at the frequencies of interest.

The DMD spectrum of **Figure 11** shows that three modes (i.e., $\boldsymbol{\Phi_8}$, $\boldsymbol{\Phi_{20}}$, $\boldsymbol{\Phi_{48}}$) are peaking above those around them



doi: 10.1016/j.ast.2021.106622

featuring oscillation frequencies of 197, 527 and 978 Hz, respectively. These frequencies are consistent with the dominant and sub-dominant frequency given by POD analysis. In fact, the spatial distributions and the modal relevance information of the dominant DMD modes (i.e., $\boldsymbol{\Phi_8}$, $\boldsymbol{\Phi_{20}}$, $\boldsymbol{\Phi_{48}}$) represented in **Figure 12** confirm and validate the correlations between frequency content and spatial morphology of the associated structures suggested by the POD energy ranking. Furthermore, these energetic modes seem to be located in a more compacted/confined region than the higher frequency ones, which seem to penetrate further downstream the combustion chamber and get more disordered.

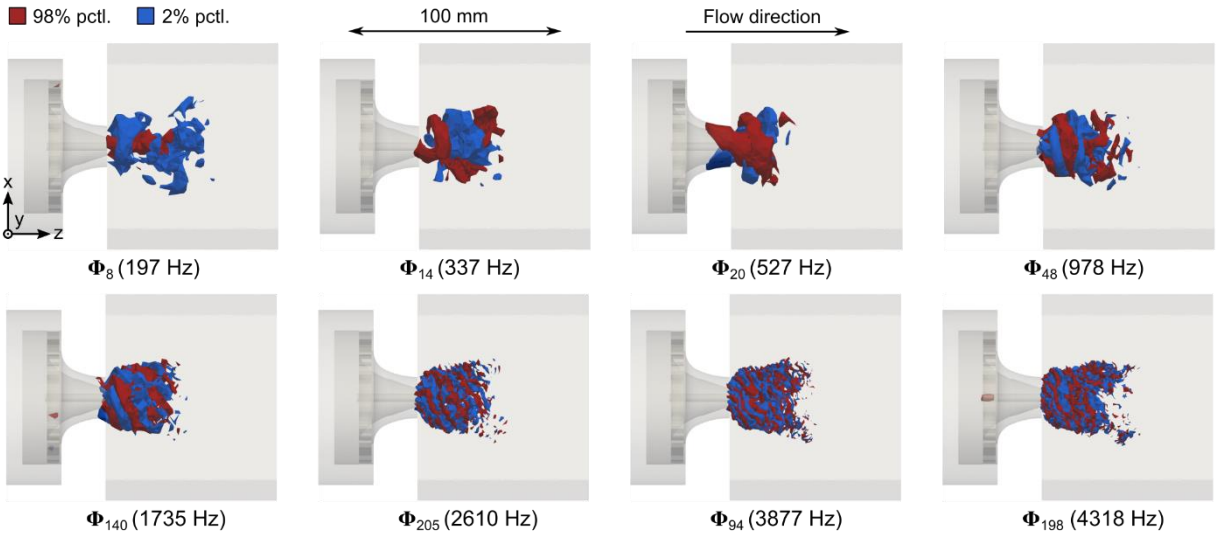


Figure 12. Spatial distribution of the eight more coherent DMD modes within the combustor. Each mode is represented by iso-surfaces indicating the 2% (blue) and 98% (red) percentiles of the spatial energy distribution of the real values of each mode $\Re\{\boldsymbol{\Phi_i}\}$.

As stated before, the benefit of DMD is that modes are organized in terms of a single frequency, unlike POD for which multiple frequencies are forced to be grouped together making the individual impact of a single frequency more difficult to discern. Hence, in addition to the main hydrodynamic PVC modes reported both in the POD analysis (**Section 4.2**) and in the literature [29, 38, 52, 66], DMD here applied also allows detecting modal structures at higher frequencies, multiples of the natural frequency -527 Hz- of the PVC (e.g., 1735 Hz, 2610 Hz, 3877 Hz and 4318 Hz), that do not respond to any previous knowledge. These higher modes show more spatial variation in the azimuthal direction (see the cross-sectional view in **Figure 13**), and a concomitant reduction in the scale of vortices when increasing frequency similar to the VBB harmonics modes reported in [67]. This seems to indicate a source flow phenomenon related to each individual channel of the swirler. Vortices appear to emanate from the swirler outlet region with decreasing vorticity towards the axial direction. In this way, spiral structures with harmonically oscillating vorticity in the streamwise direction can be identified presenting a given number of branches equal to the number of times the natural frequency of the corresponding mode.

Salvador, F.J., Carreres, M., García-Tíscar, J., Belmar-Gil, M., "Modal decomposition of the unsteady non-reactive flow field in a swirl-stabilized combustor operated by a Lean Premixed injection system", Aerospace Science and Technology 112:106622 (author version).

doi: 10.1016/j.ast.2021.106622

This can be attributed to continued formation of shear layers vortices due to the higher shear strength of the structures emanating from each of the swirler channels and its interactions with the turbulence present in the recirculation zone.

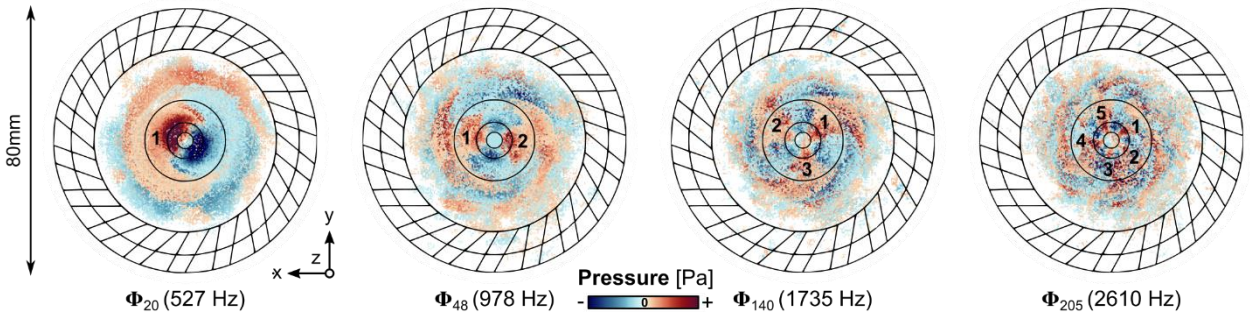


Figure 13. Frontal view of the spatial distribution of four DMD modes.

To close the discussion, the Strouhal numbers based on the main frequency peaks detected through POD and DMD are calculated. The Strouhal number of a given perturbation can be evaluated through Eq. (15):

$$St = \frac{D_{ext}\, f}{U_{Swirler}} \tag{15}$$

with $f$ the frequency of the identified structure, $D_{ext}$ the external diameter of the swirler exit and $U_{Swirler}$ the bulk velocity entering the combustion chamber from the swirler. The two peak Strouhal number are summarized in **Table 1**.

| | PVC (1st harmonic) | | | PVC (2nd harmonic) | | | VBB (CRZ generation) | | |
|---|---|---|---|---|---|---|---|---|---|
| | POD | DMD | EXP | POD | DMD | EXP | POD | DMD | EXP |
| Frequency [Hz] | 526 | 527 | 507 | 1053 | 978 | 999 | 191 | 197 | 165 |
| St [-] | 0.47 | 0.47 | 0.45 | 0.95 | 0.88 | 0.89 | - | - | - |

Table 1. Strouhal numbers for the main frequencies identified using POD and DMD techniques

Regarding the Strouhal numbers found in the literature [68], a PVC is usually found for a Strouhal number higher than 0.8. The frequency around 1000 Hz corresponding to the intermittent emergence and presence of the double-helical instability (and closely related to the single-helical instability structure detected at 500 Hz) is then identified as the main frequency of the PVC and the primary source of unsteadiness despite not having the highest amount of unsteady energy computed by POD, as shown in **Figure 8**. Therefore, the limitation of POD when attributing any physical significance to a particular frequency present in the flowfield is noted here again since some of that unsteady energy is distributed between the remaining modes instead of being grouped in a single frequency.

## 5. CONCLUSIONS



doi: 10.1016/j.ast.2021.106622

In this paper, different modal decomposition techniques have been applied to the pressure data generated by a Large Eddy Simulation to investigate the characteristics of the most powerful coherent structures of strongly swirled jets in a Lean Premixed combustor undergoing vortex breakdown. The numerical data have been post-processed through Proper Orthogonal Decomposition (POD) and Dynamic Mode Decomposition (DMD) routines to retrieve information about the flow dynamics, providing a systematic approach to identify the main mechanisms that sustain instabilities in the combustor. By considering the pressure information of the entire computational domain at once, including complex geometries such as the radial swirler, the overall amplitude for each frequency is adequately identified according to the overall unsteady energy available in the flow.

Both the POD and DMD analyses extracted similar flow dynamics results associated to a global self-excited oscillatory mode, namely the Precessing Vortex Core (PVC), having a single dominant frequency. This hydrodynamic instability mode results in double-helical vortices and leads to a counter-rotating co-winding helical structure located between the inner and the outer shear layer, enveloping the recirculation bubble. In this way, both decomposition techniques allowed detecting two distinct eigenfunctions corresponding to azimuthal wavenumbers $|m| = 1$ and $|m| = 2$, which have been found to yield a helical or double-helical breakdown mode, respectively, that dominate dynamics of the whole flow. Thus, the flow oscillations are coherent with the dominant frequency of the global mode and, taking into account the phase shift between the decomposition results, the precession of the vortex core can be attributed to the same frequency.

In addition, the DMD method implemented also allowed identifying some complex pulsating, intermittent and cyclical spatial patterns related to the harmonic helical branches of the PVC, not detected in previous investigations. In this way, spiral structures with harmonically oscillating vorticity in the streamwise direction have been identified presenting a given number of branches equal to the number of times the natural frequency of the corresponding mode. This can be attributed to the continued formation of shear layers vortices due to the higher shear strength of the structures emanating from each of the swirler channels and opens the door to specific design modifications.

In the view of the results, both the POD and the DMD have successfully extracted the flow dynamics associated with the dominant global instability mode, corresponding to a double-helical precessing vortex structure. In this way, DMD can be preferred to POD when the identification of low-energy and short-lived modes is sought. Since DMD generates a global frequency spectrum in which each mode correspond to a specific discrete frequency, its application has been demonstrated to be more efficient than POD when dealing with temporally coherent problems. Nevertheless, the price to pay is to require a more diffuse metric than in POD, raising DMD as a less appropriate option for performing Reduced-

Salvador, F.J., Carreres, M., García-Tíscar, J., Belmar-Gil, M., "Modal decomposition of the unsteady non-reactive flow field in a swirl-stabilized combustor operated by a Lean Premixed injection system", Aerospace Science and Technology 112:106622 (author version).

doi: 10.1016/j.ast.2021.106622

Order-Models (ROMs) in some circumstances. Notwithstanding, DMD technique has proved to be a robust and systematic method that can give more accurate and consistent interpretations of the periodic physics underlying hydrodynamic instabilities in the Lean Premixed combustor studied in the present investigation.

## ACKNOWLEDGEMENTS

This work was partly sponsored by the program "Ayuda a Primeros Proyectos de Investigación (PAID-06-18), Vicerrectorado de Investigación, Innovación y Transferencia de la Universitat Politècnica de València (UPV), Spain". We thankfully acknowledge the computer resources at Altamira Supercomputer and the technical support provided by Universidad de Cantabria (RES FI-2018-3-0033 and FI-2019-1-0009) in the frame of the Spanish Supercomputing Network. On the other hand, the support given to Mr. Mario Belmar by Universitat Politècnica de València through the "FPI-Subprograma 2" grant within the "Programa de Apoyo para la Investigación y Desarrollo (PAID-01-18)" is gratefully acknowledged.

## REFERENCES

[1] Madden, P. (2014). CAEP Combustion Technology Review Process and CAEP NOx Goals. In Forum-AE.

[2] Lefebvre, A. H. (1999). Gas Turbine Combustion (Taylor and Francis).

[3] Gupta, A.K., Lilley, D.G., and Syred, N. (1984). Swirl flows (Abacuss Press).

[4] Panda, J., and McLaughlin, D.K. (1994). Experiments on the instabilities of a swirling jet. Phys. Fluids, 6(1), 263–276.

[5] Billant, P., Chomaz, J., and Huerre, P. (1998). Experimental study of vortex breakdown in swirling jets. J. Fluid Mech., 376, 183-219.

[6] Chigier, N.A., and Chervinsky, A. (1967). Experimental investigation of swirling vortex motion in jets. J. Appl. Mech. 34(2), 443–451.

[7] Loève, M. (1945). Functions aleatoire de second ordre. Comptes Rendus de l'Académie des Sciences, 220.

[8] Schmid, P. J. (2010). Dynamic mode decomposition of numerical and experimental data. J. Fluid Mech., 656, 5–28.

[9] Lumley, J. L. (1967). The structure of inhomogeneous turbulence: Atmospheric turbulence and wave propagation. V.I. Tatarski Ed., 166–178.



doi: 10.1016/j.ast.2021.106622

[10] Fogleman, M., Lumley, J., Rempfer, D., and Haworth, D. (2004). Application of the proper orthogonal decomposition to datasets of internal combustion engine flows. J. Turbul., 5(23), 1–3.

[11] Danby, S., and Echekki, T. (2006). Proper orthogonal decomposition analysis of autoignition simulation data of nonhomogeneous hydrogen–air mixtures. Combust. Flame, 144(1), 126–138.

[12] Bizon, K., Continillo, G., Mancaruso, E., Merola, S., and Vaglieco, B. (2010). POD-based analysis of combustion images in optically accessible engines. Combust. Flame, 157(4), 632–640.

[13] Chen, H., Reuss, D., and Sick, V. (2011). Analysis of misfires in a direct injection engine using proper orthogonal decomposition. Exp. Fluids, 51(4), 1139–1151.

[14] Kostka, S., Lynch, A., Huelskamp, B., Kiel, B., Gord, J., and Roy, S. (2012). Characterization of flame-shedding behavior behind a bluff-body using proper orthogonal decomposition. Combust. Flame, 159(9), 2872–2882.

[15] Chen, H., Hung, D., Xu, M., Zhuang, H., and Yang, J. (2014). Proper orthogonal decomposition analysis of fuel spray structure variation in a spark-ignition direct-injection optical engine. Exp. Fluids, 55(4), 1703.

[16] Bizon, K., Continillo, G., Lombardi, S., Sementa, P., and Vaglieco, B. (2016). Independent component analysis of cycle resolved combustion images from a spark ignition optical engine. Combust. Flame, 163, 258–269.

[17] Bizon, K., Continillo, G., Mancaruso, E., Merola, S., and Vaglieco, B. (2010). Pod-based analysis of combustion images in optically accessible engines. Combust. Flame, 157(4), 632–640.

[18] Sakowitz, A., Mihaescu, M., and Fuchs, L. (2014). Flow decomposition methods applied to the flow in an IC engine manifold. Appl. Therm. Eng., 65(1), 57–65

[19] Torregrosa, A., Broatch, A., García-Tíscar, J., and Gomez-Soriano, J. (2018). Modal decomposition of the unsteady flow field in compression-ignited combustion chambers. Combust. Flame, 188, 469–482.

[20] Steinberg, A., Boxx, I., Stöhr, M., Carter, C., and Meier, W. (2010). Flow–flame interactions causing acoustically coupled heat release fluctuations in a thermo-acoustically unstable gas turbine model combustor. Combust. Flame, 157(12), 2250– 2266.

[21] Caux-Brisebois, V., Steinberg, A., Arndt, C. Meier, W. (2014). Thermoacoustic velocity coupling in a swirl stabilized gas turbine model combustor. Combust. Flame, 161(12), 3166–3180.

[22] Meadows, J., and Agrawal, A. (2015). Time-resolved piv of lean premixed combustion without and with porous inert media for acoustic control. Combust. Flame, 162(4), 1063–1077.

[23] Luo, J. (2018) Design optimization of the last stage of a 4.5-stage compressor using a pod-based hybrid model.



doi: 10.1016/j.ast.2021.106622

588 Aerosp. Sci. Technol., 76, 303–314.
589 [24] Broatch, A., García-Tíscar, J., Roig, F., and Sharma, S. (2019). Dynamic mode decomposition of the acoustic
590 field in radial compressors. Aerosp. Sci. Technol., 90, 388–400.
591 [25] Lengani, D., Simoni, D., Pichler, R., Sandberg, R., Michelassi, V., and Bertini, F. (2018). Identification and
592 quantification of losses in a LPT cascade by POD applied to LES data. Int. J. Heat Fluid Flow, 70, 28–40.
593 [26] Güner, H., Thomas, D., Dimitriadis, G., and Terrapon, V. (2019). Unsteady aerodynamic modeling methodology
594 based on dynamic mode interpolation for transonic flutter calculations. J. Fluids Struct., 84, 218–232.
595 [27] Rajpal, D., Gillebaart, E., and De Breuker, R. (2019). Preliminary aeroelastic design of composite wings
596 subjected to critical gust loads. Aerosp. Sci. Technol., 85, 96–112.
597 [28] Legrand, M., Nogueira, J., Lecuona, A., Nauri, S., and Rodríguez, P. (2010). Atmospheric low swirl burner flow
598 characterization with Stereo-PIV. Exp. Fluids, 48, 901–913.
599 [29] Oberleithner, K., Sieber, M., Nayeri, C., and Paschereit, C. (2011). Three-dimensional coherent structures in a
600 swirling jet undergoing vortex breakdown: Stability analysis and empirical mode construction. J. Fluid Mech., 679, 383–
601 414.
602 [30] Oberleithner, K., Paschereit, C., Seele, R., and Wygnanski, I. (2012). Formation of turbulent vortex breakdown:
603 Intermittency, criticality, and global instability. AIAA J., 50, 1437–1452.
604 [31] M. Percin, M. Vanierschot, B.W. Van Oudheusden, Analysis of the pressure fields in a swirling annular jet flow.
605 Exp. Fluids 58 (2017) 166.
606 [32] Alekseenko, S., Abdurakipov, S., Hrebtov, M., and Tokarev, M. (2018). Coherent structures in the near-field of
607 swirling turbulent jets: a tomographic PIV study. Int. J. Heat Fluid Flow, 70, 363–379.
608 [33] Ianiro, A., Lynch, K., Violato, D., Cardone, G., and Scarano, F. (2018). Three-dimensional organization and
609 dynamics of vortices in multichannel swirling jets. J. Fluid Mech., 843 180–210.
610 [34] Vanierschot, M., and Ogus, G. (2019). Experimental investigation of the precessing vortex core in annular
611 swirling jet flows in the transitional regime. Exp. Therm. Fluid Sci., 106, 148–158.
612 [35] Stöhr, M., Sadanandan, R., and Meier, W. (2011). Phase-resolved characterization of vortex-flame interaction in
613 a turbulent swirl flame. Exp. Fluids, 51, 1153–1167.
614 [36] Alekseenko, S., Dulin, V., Kozorezov, Y., and Markovich, D. (2012). Effect of high-amplitude forcing on
615 turbulent combustion intensity and vortex core precession in a strongly swirling lifted propane/air flame. Combust. Sci.



doi: 10.1016/j.ast.2021.106622

616 Technol., 184, 1862–1890.
617 [37] Karlis, E., Hardalupas, Y., Taylor, A. M., Rogerson, J., Sadasivuni, S., Stöhr, M., and Stopper, U. (2019).
618 Thermoacoustic phenomena in an industrial gas turbine combustor at two different mean pressures. AIAA Sci. Tech.
619 Forum, San Diego, California, 1–17.
620 [38] Cozzi, F., Sharma, R., and Solero, G. (2019). Analysis of coherent structures in the near-field region of an
621 isothermal free swirling jet after vortex breakdown. Exp. Therm. Fluid Sci., 109, 109860.
622 [39] Ruith, M., Chen, P., Meiburg, E., and Maxworthy, T. (2003). Three-dimensional vortex breakdown in swirling
623 jets and wakes: Direct numerical simulation. J. Fluid Mech., 486, 331–378.
624 [40] Huang, Y., Wang, S., and Yang, V. (2006). A systematic analysis of combustion dynamics in a lean-premixed
625 swirl-stabilized combustor. AIAA Journal, 44(4), 724–740.
626 [41] Patel, N., and Menon, S. (2008). Simulation of spray-turbulence-flame interactions in a lean direct injection
627 combustor. Combust. Flame, 153, 228–257.
628 [42] Huang, Y, and Yang, V. (2009). Dynamics and stability of lean-premixed swirl-stabilized combustion. Prog.
629 Energy Combust. Sci., 35(4), 293–364.
630 [43] Duwig, C., Ducruix, S., and Veynante, D. (2012). Studying the Stabilization Dynamics of Swirling Partially
631 Premixed Flames by Proper Orthogonal Decomposition. J. Eng. Gas Turb. and Power, 134(10), 101501.
632 [44] Grimm, F., Setzwein, F., Werner, S., Stöhr, M., Dierke, J., Ewert, R., and Aigner, M. (2019). Combustion Noise
633 Dependency on Thermal Load and Global Equivalence Ratio in a Swirl-Stabilized Combustor. AIAA Sci. Tech. Forum,
634 1–24.
635 [45] Rowley, C., Mezic, I., Bagheri, S., Schlatter, P., and Henningson, D. (2009). Spectral analysis of nonlinear flows.
636 J. Fluid Mech, 641, 115–127.
637 [46] Chen, K., Tu, J., and Rowley, C. (2012). Variants of dynamic mode decomposition: boundary condition,
638 Koopman, and Fourier analyses. J. Nonlinear Sci., 22(6), 887–915.
639 [47] Sampath, R., and Chakravarthy, S. (2016). Investigation of intermittent oscillations in a premixed dump
640 combustor using time-resolved particle image velocimetry. Combust. Flame, 172, 309–325.
641 [48] Rao, S., and Karthick, S. K. (2019). Studies on the effect of imaging parameters on dynamic mode decomposition
642 of time-resolved schlieren flow images. Aerosp. Sci. Technol., 88, 136–146.
643 [49] Lu, W., Huang, G., Wang, J., and Hong, S. (2019). Spatio–temporal dynamic mode decomposition in a shear



doi: 10.1016/j.ast.2021.106622

644 layer flow. Aerosp. Sci. Technol., 91, 263–271.
645 [50] Vinha, N., Meseguer-Garrido, F., De Vicente, J., and Valero, E. (2016). A dynamic mode decomposition of the
646 saturation process in the open cavity flow. Aerosp. Sci. Technol., 52, 198–206.
647 [51] Daroukh, M., Moreau, S., Gourdain, N., Boussuge, J., and Sensiau, C. (2019). Tonal noise prediction of a modern
648 turbofan engine with large upstream and downstream distortion. J. Turbomach., 141(2), 021010.
649 [52] Renaud, A., Tachibana, S., Arase, S., and Yokomori, T. (2018). Experimental study of thermoacoustic instability
650 triggering in a staged liquid fuel combustor using high-speed OH-PLIF. J. Eng. Gas Turbines Power, 140(8), 081505.
651 [53] Karlis, E., Liu, Y., Hardalupas, Y., and Taylor, A. (2019). H2 enrichment of CH4 blends in lean premixed gas
652 turbine combustion: An experimental study on effects on flame shape and thermoacoustic oscillation dynamics. Fuel,
653 254, 115524.
654 [54] Semlitsch, B., and Mihaescu, M. (2016). Flow phenomena leading to surge in a centrifugal compressor, Energy,
655 103 572–587.
656 [55] Kim, J. C., Jung, W. C., Hong, J. S., & Sung, H. G. (2018). The Effects of Turbulent Burning Velocity Models
657 in a Swirl-Stabilized Lean Premixed Combustor. International Journal of Turbo and Jet Engines, 35(4), 365–372.
658 [56] Cordier , M., Vandel, A., Cabot, G., Renou, B. and Boukhalfa, A. (2013). Laser-Induced Spark Ignition of
659 Premixed Confined Swirled Flames. Comb. Sci. Technol., 185(3), 379-407.
660 [57] Abdi, H., and Williams, J. (2010). Principal component analysis. Wiley Interdiscip. Rev. Comput. Stat., 2(4),
661 433–459.
662 [58] Nikiforov, V. (2007). The energy of graphs and matrices. J. Math. Anal. Appl., 326(2), 1472–1475.
663 [59] Futrzynski, R., and Efraimsson, G. (2015). Dymode: A Parallel Dynamic Mode Decomposition Software, KTH
664 Royal Institute of Technology.
665 [60] Kou, J., and Zhang, W. (2017). An improved criterion to select dominant modes from dynamic mode
666 decomposition. J. Mech. B. Fluids, 62, 109–129.
667 [61] CONVERGE 2.4 Manual. Convergent Science, Inc., Middleton, 2017.
668 [62] Payri R, Novella R, Carreres M, et al. (2020). Modeling gaseous non-reactive flow in a lean direct injection gas
669 turbine combustor through an advanced mesh control strategy. Proc IMechE Part G: J Aerospace Engineering 234(11),
670 1788–1810.
671 [63] Bentley, J. (1975). Multidimensional binary search trees used for associative searching. Commun. ACM, 18(9),



doi: 10.1016/j.ast.2021.106622

509–517.

[64] Friedman, J., Bentley, J. and Finkel, R. (1977). An algorithm for finding best matches in logarithmic expected time. ACM Trans. Math. Softw., 3(3), 209–226.

[65] Ivanic T, Foucault E and Pecheux J. (2003). Dynamics of swirling jet flows. Exp Fluids, 35(4), 317–324.

[66] Cordier, M. (2013). Allumage et propagation de flamme dans les écoulements fortement swirlés:études expérimentales et numériques. PhD Thesis, INSA.

[67] Huang, C., Gejji, R., and Anderson, W. (2014). Combustion Dynamics Behavior in a Single-Element Lean Direct Injection (LDI) Gas Turbine Combustor. In: 50th AIAA/ASME/SAE/ASEE Joint Prop. Conf., Cleveland, United States.

[68] Syred, N. (2006). A review of oscillation mechanims and the role of the precessing vortex core in swirl combustion systems. Prog. Energy Comb. Sci., 32(2), 93–161.

Salvador, F.J., Carreres, M., García-Tíscar, J., Belmar-Gil, M., “Modal decomposition of the unsteady non-reactive flow field in a swirl-stabilized combustor operated by a Lean Premixed injection system”, Aerospace Science and Technology 112:106622 (author version).

doi: 10.1016/j.ast.2021.106622